Check for updates

ADVANCED MATERIALS
www.advmat.de

Size-Dependent Photocatalytic Reactivity of Conjugated Microporous Polymer Nanoparticles

Seunghyeon Kim, Xin Zhou, Yungui Li, Qiqi Yang, Xiaomin Liu, Robert Graf, Paul W. M. Blom, Calum T. J. Ferguson, and Katharina Landfester**

Particle size is a critical factor for improving photocatalytic reactivity of conjugated microporous polymers (CMPs) as mass transfer in the porous materials is often the rate-limiting step. However, due to the synthetic challenge of controlling the size of CMPs, the impact of particle size is yet to be investigated. To address this problem, a simple and versatile dispersion polymerization route that can synthesize dispersible CMP nanoparticles with controlled size from 15 to 180 nm is proposed. Leveraging the precise control of the size, it is demonstrated that smaller CMP nanoparticles have dramatically higher photocatalytic reactivity in various organic transformations, achieving more than 1000% enhancement in the reaction rates by decreasing the size from 180 to 15 nm. The size-dependent photocatalytic reactivity is further scrutinized using a kinetic model and transient absorption spectroscopy, revealing that only the initial 5 nm-thick surface layer of CMP nanoparticles is involved in the photocatalytic reactions because of internal mass transfer limitations. This finding substantiates the potential of small CMP nanoparticles to efficiently use photo-generated excitons and improve energy-efficiency of numerous photocatalytic reactions.

1. Introduction

Conjugated microporous polymers (CMPs) have shown great potential as versatile organic heterogeneous photocatalysts because their properties can be finely tuned for individual photocatalytic applications to maximize the photocatalytic reactivity.[1–3] This limitless customization is powered by the availability of various cross-coupling protocols and monomers.[1,4] Judicious selection of reaction conditions and monomers has enabled not only the precise control of the optical and electrochemical properties of CMPs[5–7] but also improvements in their conjugation length,[8] charge separation,[9,10] porosity,[11] and wettability[12] for accomplishing enhanced photocatalytic reactivity.

Particle size is another important factor for optimizing the photocatalytic reactivity of CMPs.[1,12] To date, the impact of particle size has been underexplored due to the lack of practical synthetic methods for controlling the size of CMPs; while, ensuring good dispersibility. As a result, they are usually µm-scale particles, whose large size can prevent the cores from absorbing light especially when the CMPs have short light penetration depth (<200 nm, e.g., absorption coefficient >5 × 10^4 cm^{-1}) (**Scheme 1a**). Recently, the formation of CMP nanoparticles has been achieved by miniemulsion methods;[13–15] thereby, solving the light penetration problem.

The photocatalytic reactivity of CMP nanoparticles can still be limited by hindered substrate diffusion through the porous materials. In order for the photocatalytic reactions to occur, substrates should meet photo-generated excitons or charge carriers in the CMP nanoparticles. Therefore, the diffusion rates of substrates from the bulk to the surface and inside the CMP nanoparticles can significantly impact overall reaction dynamics. Particularly, substrate diffusion in the microporous materials can be significantly hindered by interactions between the diffusing molecule and the pore wall.[16,17] If the rate of substrate diffusion through the porous nanoparticles is slow compared to the photocatalytic reaction rate, that is, if the Thiele modulus (φ) > 1,[18] the substrates can be consumed (A → B) before accessing the photo-generated excitons from inner cores, making the cores inactive for photocatalysis (Scheme 1b). In extreme cases ($\varphi \gg 1$), only the thin surface layer of the CMP nanoparticles can be active as a photocatalyst because the exciton diffusion length in conjugated polymers is typically less than 20 nm within their lifetime (< 1 ns).[19,20] In other words, the thin outer shell of the nanoparticles can act as a very efficient photocatalyst despite the diffusional resistance of substrates in the porous materials. Thus, we propose to decrease the size of CMP nanoparticles for improving their photocatalytic reactivity because small CMP nanoparticles

S. Kim, X. Zhou, Y. Li, Q. Yang, X. Liu, R. Graf, P. W. M. Blom, C. T. J. Ferguson, K. Landfester
Max Planck Institute for Polymer Research
Ackermannweg 10, 55128 Mainz, Germany
E-mail: c.ferguson.1@bham.ac.uk; landfest@mpip-mainz.mpg.de
C. T. J. Ferguson
School of Chemistry
University of Birmingham
Edgbaston, Birmingham B15 2TT, UK

The ORCID identification number(s) for the author(s) of this article can be found under https://doi.org/10.1002/adma.202404054

© 2024 The Author(s). Advanced Materials published by Wiley-VCH GmbH. This is an open access article under the terms of the Creative Commons Attribution-NonCommercial License, which permits use, distribution and reproduction in any medium, provided the original work is properly cited and is not used for commercial purposes.

DOI: 10.1002/adma.202404054

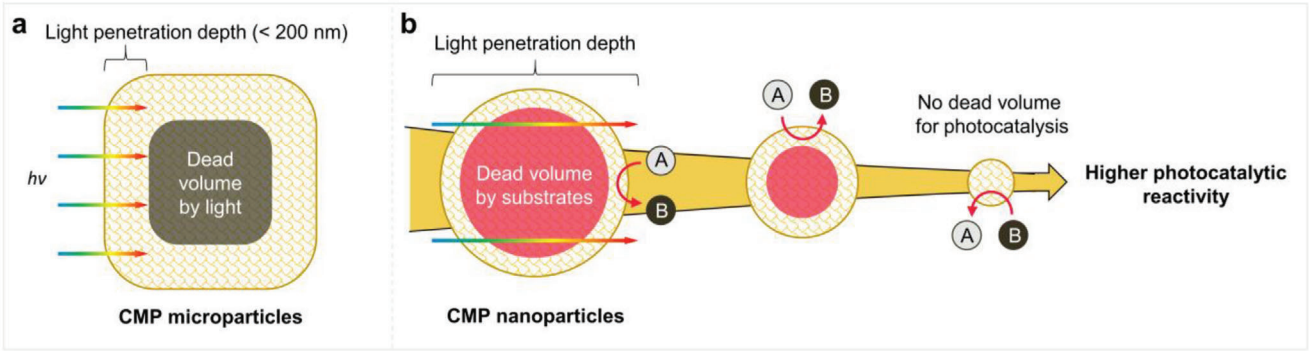

Scheme 1. Dead volume in conjugated microporous polymer (CMP) particles by accessibility of a) light and b) substrates. Only the thin outer shell of CMP particles can be active as a photocatalyst. Thus, decreasing the particle size can reduce the dead volume, achieving higher photocatalytic reactivity.

would have less dead volume and use the absorbed photons more efficiently for photocatalysis (Scheme 1b).

To achieve this goal, a new synthetic route needs to be developed to prepare CMP nanoparticles with both good dispersibility and controlled size. Particularly, good colloidal stability is important to prevent aggregation of the nanoparticles. In this regard, we have recently established the concept of hairy CMP nanoparticles,[15] where covalently bonded polymeric hairs provide permanent steric stabilization for the nanoparticles. As for the size-controlled synthesis of the CMP nanoparticles, dispersion polymerization is a promising approach because it can control the size of dispersible polymeric particles by using different chain lengths and concentrations of dispersants.[21] Moreover, the dispersion polymerization is compatible with polycondensation reactions such as C—C cross-coupling reactions,[22–24] so it can be applied to create photocatalytic CMP nanoparticles.

Therefore, we implemented the dispersion polymerization approach to synthesize well-dispersible CMP nanoparticles with controlled size by cross-coupling tri- and di-functional monomers with polymeric dispersants (**Scheme 2a**). In this blueprint, the cross-coupling reactions were initiated in the homogeneous mixture of CMP monomers and polymeric dispersants. The insoluble oligomers aggregated and polymerized until the resulting CMP particles were sterically stabilized by a sufficient number of the dispersants on their surface. The permanent steric stabilization of the CMP particles would be achieved at smaller size upon using longer chain lengths and higher concentrations of the dispersants, generating the CMP nanoparticles with smaller CMP cores (Scheme 2b).

To verify the size-controlling principle, we employed different chain lengths and concentrations of polymeric dispersants to synthesize different sizes of CMP nanoparticles via Sonogashira–Hagihara coupling.[25] We then investigated the impacts of the particle size, optical and electrochemical properties, and wetted surface area of CMP nanoparticles on photocatalytic thiol-ene coupling reaction. The photocatalytic reaction rates exhibited a strong inverse correlation with the core size of CMP nanoparticles. Notably, the smallest cores (<20 nm) presented an order of magnitude faster reaction rates than the largest cores (≈180 nm), which supports the hypothesis that the photocatalytic reactivity of CMP nanoparticles can be enhanced by decreasing their size. From the size–photocatalytic reactivity relationship, we also estimated the thickness of the photocatalytic shell to be ≈5 nm. Transient absorption spectroscopy data suggest that this shell thickness is mainly attributed to substrate diffusion in the CMP nanoparticles because no exciton diffusion was observed. Finally, we demonstrated that the size-controlled synthesis of CMP nanoparticles could be achieved with other cross-coupling

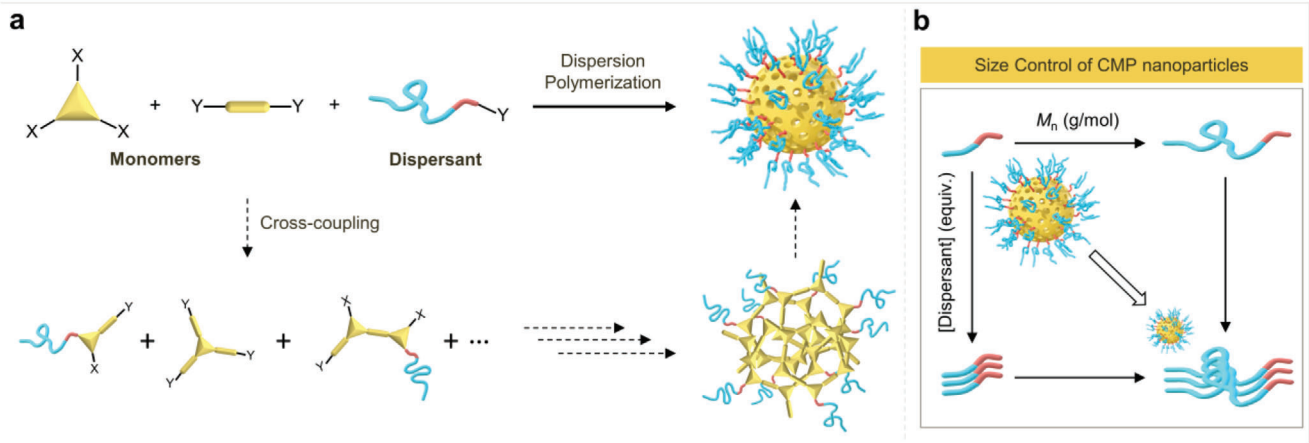

Scheme 2. a) Proposed scheme for size-controlled synthesis of CMP nanoparticles via dispersion polymerization and b) size-controlling principle using chain lengths and concentrations of dispersants.

© 2024 The Author(s). Advanced Materials published by Wiley-VCH GmbH

15214095, 2024, 35, Downloaded from https://onlinelibrary.wiley.com/doi/10.1002/adma.202404054 by MPI 355 Polymer Research, Wiley Online Library on [02/10/2024]. See the Terms and Conditions (https://onlinelibrary.wiley.com/terms-and-conditions) on Wiley Online Library for rules of use; OA articles are governed by the applicable Creative Commons License

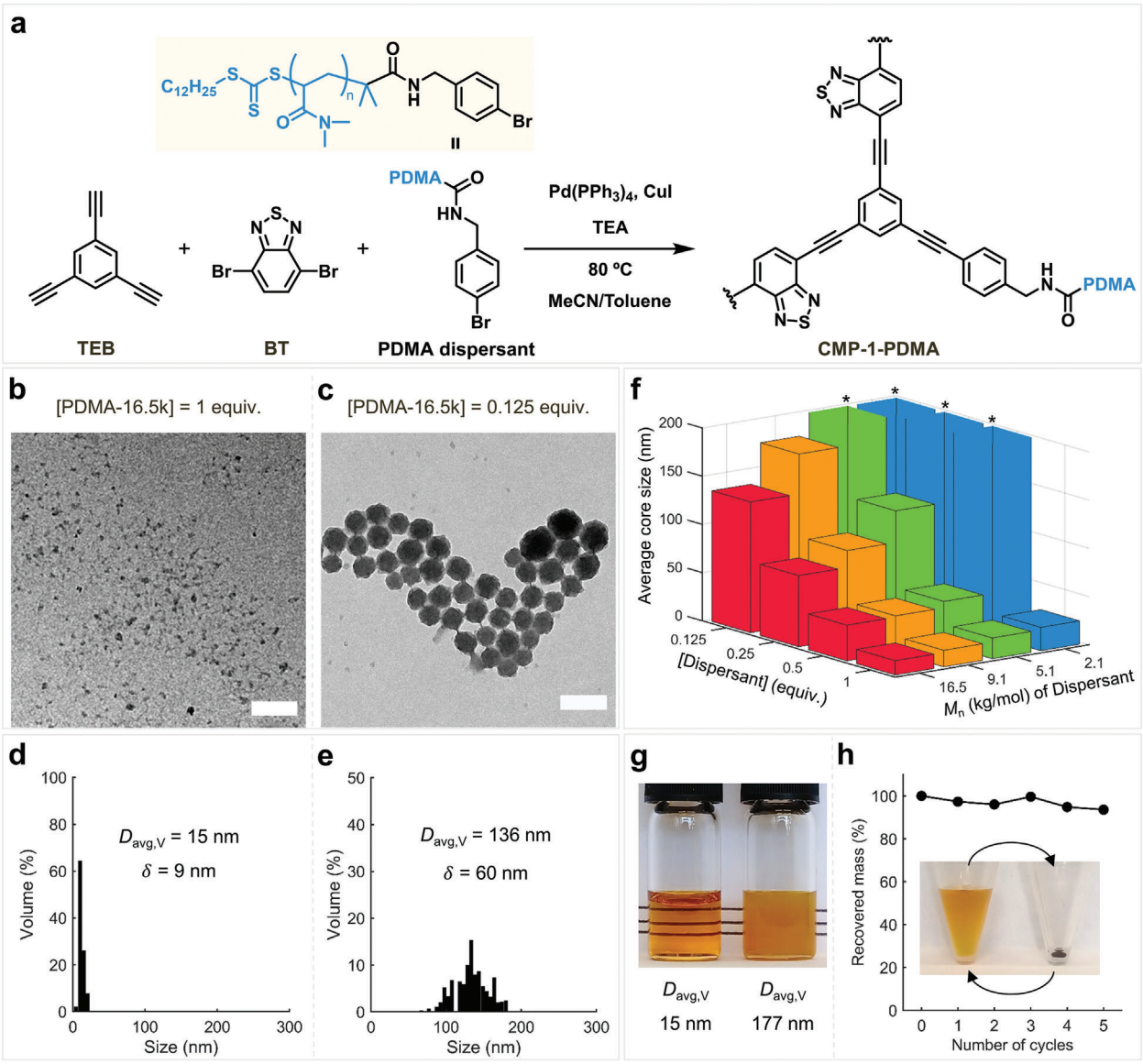

Figure 1. Size-controlled synthesis of CMP nanoparticles via Sonogashira–Hagihara coupling. a) Reaction scheme for the synthesis of CMP-1-PDMA. Different chain lengths (M_n = 2.1, 5.1, 9.1, or 16.5 kg mol^{-1}) and concentrations (1, 0.5, 0.25, or 0.125 equiv.) of PDMA dispersants formed homogeneous mixtures with 2.5 equiv. of TEB and 3.5 equiv. of BT, before initiating the cross-coupling reaction. b,c) TEM images of CMP-1-PDMA prepared with 1 equiv. or 0.125 equiv. of PDMA-16.5k. Scale bar: 200 nm. d,e) Volume-weighted core size distribution of CMP-1-PDMA prepared with 1 equiv. or 0.125 equiv. of PDMA-16.5k. $D_{avg,V}$ and δ represent the volume-weighted mean diameter and width of the distribution, respectively. f) Volume-weighted mean diameters of CMP cores of CMP-1-PDMAs. Four conditions marked with asterisks produced μm-scale CMP particles with irregular shapes. g) Dispersibility of CMP nanoparticles with the smallest CMP cores ([PDMA-16.5k] = 1 equiv.) and the largest CMP cores ([PDMA-9.1k] = 0.125 equiv.). h) Recovery test of CMP nanoparticles with the smallest CMP cores ($D_{avg,V}$ = 15 nm).

protocols such as Suzuki–Miyaura coupling and confirmed the size-dependent photocatalytic reactivity with different CMP nanoparticles in various photocatalytic dehalogenative transformations of aryl halides.

2. Results and Discussion

To demonstrate the size-controlled synthesis of CMP nanoparticles, we first explored the Sonogashira–Hagihara coupling to synthesize CMP-1-PDMAs with 1,3,5-triethynylbenzene (TEB), 4,7-dibromo-2,1,3-benzothiadiazole (BT), and polymeric dispersants (**Figure 1a**). For the dispersants, we employed four different chain lengths (M_n = 2.1, 5.1, 9.1, and 16.5 kg mol^{-1}) of poly(*N*,*N*-dimethylacrylamide) (PDMA) with 4-bromophenyl groups on the α-end of the RAFT polymers (Figures S1–S5 and Tables S1 and S2, Supporting Information), which are denoted by PDMA-2.1k, −5.1k, −9.1k, and −16.5k, respectively. Notably, the mixture of acetonitrile (MeCN) and toluene was used as a solvent for the synthesis of CMP-1-PDMAs to completely dissolve the monomers and the PDMA dispersants. The concentrations

© 2024 The Author(s). Advanced Materials published by Wiley-VCH GmbH

15214095, 2024, 35, Downloaded from https://onlinelibrary.wiley.com/doi/10.1002/adma.202404054 by MPI 355 Polymer Research, Wiley Online Library on [02/10/2024]. See the Terms and Conditions (https://onlinelibrary.wiley.com/terms-and-conditions) on Wiley Online Library for rules of use; OA articles are governed by the applicable Creative Commons License

of triethylamine (TEA) and the monomers were also optimized to enhance the cross-coupling kinetics (Figures S6–S10, Supporting Information). With the optimized protocol, we prepared 16 different CMP-1-PDMAs using each of the four PDMA dispersants at four different concentrations (1, 0.5, 0.25, and 0.125 equiv.) (Tables S3 and S4, Supporting Information). The resulting CMP-1-PDMAs are denoted in this paper by the concentrations (e.g., [PDMA-16.5k] = 1 equiv.) of the dispersants used for their synthesis.

The chemical structures of CMP-1-PDMAs shown in Figure 1a were confirmed by solid-state ^{13}C cross-polarization magic-angle spinning (CP-MAS) nuclear magnetic resonance (NMR) spectroscopy and Fourier transform infrared (FT-IR) spectroscopy. The solid-state ^{13}C NMR spectra of CMP-1-PDMAs showed identical acetylene carbon and aromatic carbon signals regardless of the chain lengths and concentrations of the PDMA dispersants used for the synthesis of the materials (Figure S11, Supporting Information). These carbon signals from the CMP networks were also consistent with reported values for CMP-1 prepared without a PDMA dispersant in the literature,[26] demonstrating that the PDMA dispersants were not obstructing the formation of the CMP networks in CMP-1-PDMAs. As expected, the carbon signals from the PDMA dispersants increased with their amounts used for the synthesis of CMP-1-PDMAs. The solid-state NMR results were complemented by the FT-IR spectra of CMP-1-PDMAs, which featured the characteristic absorptions by the CMP networks (C═C bending, C═C stretching, C≡C stretching, and C≡C—H stretching) although the IR signals from the CMP networks decreased as the PDMA weight fractions increased in CMP-1-PDMAs (Figures S12–S14, Supporting Information). Comparing with the reference FT-IR spectrum of the PDMA dispersant, we also confirmed that the PDMA chains were intact during the formation of CMP-1-PDMAs.

The core size and morphologies of CMP-1-PDMAs were examined by transmission electron microscopy (TEM) (Figures S15–S18, Supporting Information). As highlighted in Figure 1b–e, the combination of the longest chain length (PDMA-16.5k) and the highest concentration (1 equiv.) produced very small nanoparticles, whose volume-weighted mean diameter ($D_{avg,V}$) was 15 nm while the same PDMA dispersant at the lowest concentration (0.125 equiv.) yielded large nanoparticles with a $D_{avg,V}$ of 136 nm. It should be noted that these CMP-1-PDMAs were spherical nanoparticles as opposed to ring-shaped particles which were obtained by the miniemulsion method[14] with the same monomers, TEB and BT. This result highlights the importance of the permanent steric stabilization in controlling the nanoparticle formation. When the particle stabilization was not sufficient during the synthesis because of too short chain length (PDMA-2.1k) and low concentrations (0.5–0.125 equiv.), uncontrolled aggregation occurred, resulting in CMP microparticles with irregular shapes (Figure S15, Supporting Information). Therefore, we excluded these μm-sized CMP particles in the particle size analysis. Other CMP-1-PDMAs showed that they had cores ranging from 15 to 180 nm (Figure S19, Supporting Information). The average core size successfully demonstrated that longer chain lengths and higher concentrations of the PDMA dispersants produced smaller CMP cores (Figure 1f), which verifies the size-controlling principle of dispersion polymerization (Scheme 2b). In addition, we confirmed linear correlations between the average core size and the reciprocal of dispersant concentration used for the synthesis of CMP-1-PDMAs (Figure S20, Supporting Information). This linear relationship is consistent with conventional dispersion polymerization.[21]

The hydrodynamic size distributions of CMP-1-PDMAs also substantiated the claim that dispersion polymerization can control the size of the CMP nanoparticles using the dispersant concentrations (Figure S21, Supporting Information). All CMP nanoparticles showed narrow size distributions (PDI ≤ 0.2, except for [PDMA-2.1k] = 1 equiv. of PDI = 0.26), and the more dispersants yielded the smaller hydrodynamic size. However, longer chain lengths did not always result in smaller hydrodynamic size because the length of dispersants on the surface of CMP cores could contribute to the hydrodynamic size of CMP-1-PDMAs. Therefore, we used the average core size from the TEM images to analyze the impact of particle size on the photocatalytic reactivity of CMP nanoparticles.

In addition to the size control, the dispersion polymerization protocol provided facile access to CMP nanoparticles with solvent-specific dispersibility. On the one hand, the covalently bonded PDMA dispersants were soluble in polar organic solvents such as *N*-methyl-2-pyrrolidone (NMP) and *N*,*N*-dimethylformamide, so the CMP-1-PDMAs showed good dispersibility and colloidal stability in those solvents irrespective of the size of the CMP cores (Figure 1g). On the other hand, the PDMA dispersants were not soluble in non-polar solvents such as n-hexane. Thus, even the smallest CMP nanoparticles ([PDMA-16.5k] = 1 equiv., $D_{avg,V}$ = 15 nm) could be easily recovered by 1 min of centrifugation at 3000 × *g* with the mixture of 15% toluene/85% n-hexane (Figure S22, Supporting Information). Interestingly, the recovered CMP nanoparticles could be dispersed and precipitated four more times without losing the materials significantly (<6%) (Figure 1 h; Figure S23, Supporting Information).

Although the permanent solvent-specific dispersibility was achieved by incorporating the dispersant chain end into the CMP network, the photophysical and electrochemical properties of CMP-1-PDMAs showed minimal change. This was crucial for investigating the independent impact of particle size on the photocatalytic reactivity of CMP nanoparticles. UV–vis absorbance spectra of CMP-1-PDMAs revealed that all CMP nanoparticles had similar absorption maximum at 400–460 nm (Figure S24, Supporting Information). The optical band gap energy (E_g) of CMP-1-PDMAs decreased with the concentrations of the dispersants (Figures S25 and S26 and Table S5, Supporting Information), likely because less phenyl groups were incorporated into the CMP network (Figure S27, Supporting Information), but the values were still distributed in the narrow range from 2.42 to 2.52 eV. CMP-1-PDMAs prepared with 1 equiv. of the PDMA dispersants exhibited the maximum photoluminescence at 544 nm, and the peaks were blue-shifted only by 8 nm, at most, when the samples were prepared with 0.125 equiv. of the dispersants (Figure S28, Supporting Information). Moreover, cyclic voltammetry (CV) measurements revealed no correlation between the reduction onset potential of CMP-1-PDMAs and the concentrations of the PDMA dispersants used for their synthesis (Figures S29 and S30, Supporting Information). From the onset potential and optical band gap energy, the HOMO and LUMO energy levels

© 2024 The Author(s). Advanced Materials published by Wiley-VCH GmbH

15214095, 2024, 35, Downloaded from https://onlinelibrary.wiley.com/doi/10.1002/adma.202404054 by MPI 355 Polymer Research, Wiley Online Library on [02/10/2024]. See the Terms and Conditions (https://onlinelibrary.wiley.com/terms-and-conditions) on Wiley Online Library for rules of use; OA articles are governed by the applicable Creative Commons License

of CMP-1-PDMAs were estimated to be +1.50 to +1.64 V vs SCE and −0.85 to −0.97 V vs SCE (Tables S6 and S7, Supporting Information). These small variations in the redox potential suggested that the size-controlled synthesis of CMP nanoparticles induced negligible modification to the electrochemical properties of the CMP cores.

Using the CMP nanoparticles with different size, we investigated the impacts of their core size on the photocatalytic reaction rates. To compare the photocatalytic reactivity of the CMP cores in different CMP-1-PDMAs, we first measured the weight fractions of the CMP cores using thermogravimetric analysis (Figures S31 and S32 and Tables S8 and S9, Supporting Information) and used the same amount of CMP cores (e.g., 0.5 mg) (Table S10, Supporting Information) in each reaction. As a model photocatalytic reaction, we developed a photocatalytic thiol-ene coupling reaction of methyl 3-mercaptopropionate and allyl hexanoate (**Figure 2a**; Tables S11–S13, Supporting Information). The thiol-ene reaction s a well-established click-type hydrothiolation of alkenes. The reaction has been widely employed to prepare near-perfect polymer networks because it proceeds quantitatively under various conditions, including a radical pathway.[27] Particularly, the photocatalytic radical pathways are tolerant to oxygen and moisture and proceed with both metal-based photocatalysts[28,29] and metal-free organic photocatalysts[30] in many solvents such as water, MeCN, and NMP that can dissolve PDMA. Therefore, this model reaction would be suitable for investigating the impact of particle size on photocatalytic reactivity. Control experiments confirmed that both photocatalyst and light were essential for the transformation and that triethanolamine (TEOA) could accelerate the reaction (Table S14, Supporting Information). Interestingly, stronger inorganic bases than TEOA ($pK_a = 7.74$), such as NaOH and K_2CO_3, resulted in negligible product yields although the pK_a values of their conjugate acids are high enough to dissociate the thiol ($pK_a = 9.17$, predicted) (Table S15, Supporting Information). These results were consistent with literature[31] and indicate that TEOA did not behave as a base catalyst to generate a more easily oxidized thiolate but mediated the one-electron oxidation and deprotonation of the thiol (Figure S33, Supporting Information). Notably, the use of NMP as a non-volatile solvent and TEOA as an efficient redox mediator could prevent undesired solvent loss during N_2 purging and achieve rapid reaction kinetics only in the presence of photocatalysts, thus improving the accuracy of kinetic analysis. Furthermore, we carefully chose the photocatalyst concentration (0.5 mg CMP cores/mL NMP) to enable semiquantitative comparisons between different CMP nanoparticles under the same light intensity and fixed photoreactor geometry (Figure S34, Supporting Information).[32]

The kinetic analysis successfully demonstrated that the photocatalytic reaction rates increased as the core size of CMP-1-PDMAs decreased (Figure 2b). Surprisingly, the smallest CMP cores ($D_{avg,V} = 15$ nm) achieved 1100% enhancement in the reaction rates compared to the largest CMP cores ($D_{avg,V} = 177$ nm), and even, 1700% enhancement compared to the μm-sized CMP particles ([PDMA-2.1k] = 0.25 and 0.125 equiv.) (Figure S35, Supporting Information). The strong inverse correlation between the reaction rates and the size of CMP cores was also consistent with our hypothesis that the photocatalytic reactivity of CMP nanoparticles could be improved by decreasing their size to reduce the dead volume (Scheme 1b). Gratifyingly, we found that a simple mathematical model based on the hypothesis could explain the relationship between the reaction rates and the size (D) of CMP cores and even estimate the thickness (L) of the photocatalytic shell that was mainly contributing to photocatalysis (Figure 2c). When the substrate diffusion is too slow compared to reaction rates in the porous photocatalyst, that is, when Thiele modulus (φ) $\gg 1$, substrates can be depleted near the outer surface of CMP cores and only the excitons nearby this reaction-diffusion layer can contribute to the photocatalysis. In this case, the reaction rates per unit mass or volume of the photocatalysts should be proportional to the ratio of the shell volume (V_s) to the core volume (V_c), which is mathematically given by the third order polynomials of $6/D$. This model fit very well the reaction rate data in Figure 2b, and by comparing the ratios of the polynomial coefficients in the model and the fitted curve (Table S16, Supporting Information), the thickness of the photocatalytically active shell could be estimated to be ≈5 nm.

Considering that conjugated polymers often have exciton diffusion lengths in the range from 5 to 20 nm,[19,20] the 5-nm thick effective photocatalytic shell might indicate that substrates are depleted by excitons near the surface before penetrating into the CMP nanoparticles. To clarify the roles of exciton and substrate diffusion played during the photocatalysis, we used transient absorption spectroscopy to investigate excited state dynamics of CMP-1-PDMAs ([PDMA-16.5k] = 1, 0.5, 0.25, and 0.125 equiv.). As shown in Figure 2d,e, transient absorption spectra of [PDMA-16.5k] = 1 equiv. featured ground state bleaching below 450 nm and a broad absorption band around 600 nm, which extended from 450 nm to the near-IR wavelength. On the ps time scale, the absorption band decayed with the peak blue-shifted from 625 to 600 nm. Meanwhile, the kinetic trace could not be fully explained by one-term and two-term exponential curve fitting (Figure S36, Supporting Information). Interestingly, a broad, non-specific near-IR absorption band (1000–1500 nm) showed a faster decay than the absorption band at ≈600 nm (Figure S36, Supporting Information). The global analysis of transient absorption data indicates that the absorption at 600 nm stemmed from at least two transient species. None of them was a triplet exciton because the transient signals decayed at the same rate under both air and N_2 atmosphere (Figure S37, Supporting Information) while no long-lived transient species were observed.

For the following reasons, we speculated that the major species for the absorption band at 600 nm are polaron pairs. First, the absorption band exhibited higher ΔA around 600 nm upon addition of TEOA as a sacrificial electron donor under N_2 atmosphere (Figure S38, Supporting Information). The enhanced peak absorbance may indicate that the absorption band around 600 nm was partially attributed to negative polarons generated by the electron transfer from TEOA to the CMP nanoparticles.[33] However, the fast rise (<1 ps) of the band in the absence of TEOA (Figure 2e) implies that it is more likely related to a polaron pair than fully separated charges because polaron pairs can be formed in a time much shorter than a ps,[34–36] and they can show very similar spectral features to those of free polarons.[33,34,37] Second, the transient decay kinetics was independent of the excitation fluences (Figure 2f). Under the excitation conditions (12.5, 25.0, and 50.0 μJ cm^{-2}), initial number densities (N_i) of excitons generated by one pump pulse were estimated to be 5.34×10^{13} cm^{-3},

© 2024 The Author(s). Advanced Materials published by Wiley-VCH GmbH

15214095, 2024, 35, Downloaded from https://onlinelibrary.wiley.com/doi/10.1002/adma.202404054 by MPI 355 Polymer Research, Wiley Online Library on [02/10/2024]. See the Terms and Conditions (https://onlinelibrary.wiley.com/terms-and-conditions) on Wiley Online Library for rules of use; OA articles are governed by the applicable Creative Commons License

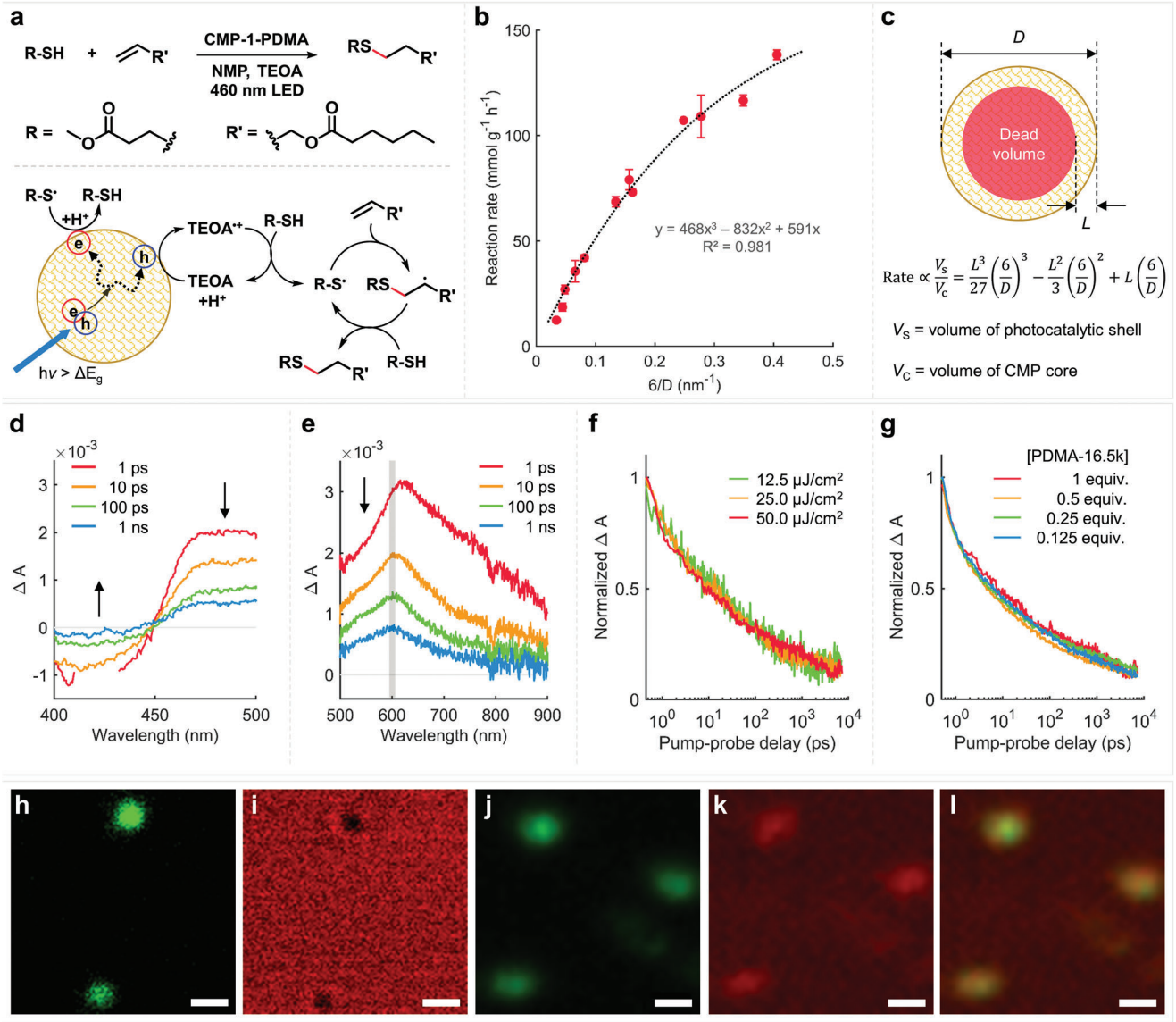

Figure 2. Size-dependent photocatalytic reactivity of CMP-1-PDMAs. a) Reaction scheme and proposed mechanism for the photocatalytic thiol-ene coupling reaction of methyl 3-mercaptopropionate and allyl hexanoate. NMP: *N*-methyl-2-pyrrolidone. TEOA: triethanolamine. b) Relationship between the reaction rates per g of CMP cores (mmol g^{-1} h^{-1}) and the CMP core size (*D*, nm) of CMP-1-PDMAs. The error bars were obtained from four replicates. c) Theoretical calculation of the volumetric ratio of the photocatalytic shell to the CMP cores, which is proportional to the reaction rates per g of CMP cores. *D* is the diameter of the CMP cores and *L* is the thickness of the photocatalytic shell. Transient absorption spectra of the [PDMA-16.5k] = 1 equiv. dispersion under N_2 atmosphere at four pump–probe delay times when excited at d) 360 nm, 50 μJ cm^{-2} and e) 400 nm, 50 μJ cm^{-2}. f) Normalized transient absorption decays of the [PDMA-16.5k] = 1 equiv. dispersion probed at 600 nm with different fluences (12.5, 25.0, and 50.0 μJ cm^{-2}). g) Normalized transient absorption decays of CMP-1-PDMA dispersions probed at 600 nm. The laser fluence was 50 μJ cm^{-2}. h,i) Confocal images of [PDMA-16.5k] = 0.125 equiv. (green) incubated with Alexa Fluor 647 (red) in water. Scale bar: 500 nm. The hydrophilic fluorophore cannot diffuse into the CMP cores. j,k) Confocal images and l) merge image of [PDMA-16.5k] = 0.125 equiv. (green) incubated with PMIM-OH (red) in $CHCl_3$. Scale bar: 500 nm. The hydrophobic fluorophore can diffuse into the CMP cores.

1.07×10^{14} cm^{-3}, and 2.14×10^{14} cm^{-3}, respectively, by using $N_i = \epsilon Pc/A_p E_{ph}$.[38] Here, ϵ is the ground-state extinction coefficient (mol^{-1} cm^2), *P* is the per-pulse energy of the pump (J), *c* is the ground-state concentration of potential exciton sites (mol cm^{-3}), A_p is the spot area of the pump beam (cm^2), and $E_{ph} = h\nu$ is the single-photon energy (J).[38] For the dispersion, the density (N_{gr}) of potential exciton sites in the ground state was estimated to be 1.37×10^{16} cm^{-3}. The estimated exciton densities were high enough to induce bimolecular exciton annihilation in organic semiconductors.[38,39] Therefore, this fluence-independent decay strongly suggests that the relevant transient species could not freely migrate; and thus, decay by a monomolecular process such as geminate recombination, which is a common feature of polaron pairs.[35–37] Third, the observed blue-shift of the absorption band from 625 to 600 nm may be due to the Coulomb interaction between the oppositely charged polaron pairs formed on adjacent

© 2024 The Author(s). Advanced Materials published by Wiley-VCH GmbH

15214095, 2024, 35, Downloaded from https://onlinelibrary.wiley.com/doi/10.1002/adma.202404054 by MPI 355 Polymer Research, Wiley Online Library on [02/10/2024]. See the Terms and Conditions (https://onlinelibrary.wiley.com/terms-and-conditions) on Wiley Online Library for rules of use; OA articles are governed by the applicable Creative Commons License

chains,[40] which could occur even in amorphous samples.[41] Lastly, the photo-induced absorption below the optical band gap energy (≈2.5 eV, 495 nm) supports the presence of localized electronic states in the gap, which is consistent with the formation of polaron pairs. When a polaron forms, the local lattice around the electron or hole gets distorted, creating an electronic state that is lower in energy than the conduction band minimum or higher in energy than the valence band maximum, respectively.[42,43] Upon excitation of the CMP nanoparticles, the resulting electron and hole could be rapidly trapped in these two localized states, which could reduce the energy band gap. In light of the aforementioned evidence, we assigned the absorption band at 600 nm to polaron pairs.

The transient absorption spectroscopy data imply that most of the singlet excitons in the CMP nanoparticles ([PDMA-16.5k] = 1 equiv.) rapidly form immobile polaron pairs within sub-ps time scale. The fast and efficient generation of polaron pairs demonstrates that the exciton diffusion plays a minor role during the photocatalysis in the CMP nanoparticles. Other CMP-1-PDMAs ([PDMA-16.5k] = 0.5, 0.25, and 0.125 equiv.) with larger CMP cores also presented the same spectral features (Figure S39, Supporting Information) and fluence-independent decays (Figure S40, Supporting Information). Particularly, the excited state dynamics of CMP-1-PDMAs were independent of the CMP core size (Figure 2g). These results confirmed that the size-dependent photocatalytic reactivity of CMP-1-PDMAs did not originate from the different dynamics of photo-generated transient species in these nanoparticles. Therefore, the 5-nm thick effective photocatalytic shell can be mainly attributed to slow substrate diffusion compared to fast photocatalytic reactions in the porous photocatalyts, that is, Thiele modulus (φ) ≫ 1. The transient absorption spectroscopy results are consistent with the interpretation that the internal mass transfer limitations allow only the thin surface layer of the CMP nanoparticles to actively contribute to photocatalysis.

It should be noted that this conclusion is only valid in cases when the substrates can diffuse into the CMP cores. According to the estimated pore size distribution, the CMP nanoparticles are mesoporous (Figures S41 and S42, Supporting Information) so that small-molecule substrates can diffuse into the porous network. Using confocal imaging, we successfully demonstrated that a hydrophobic fluorophore (PMIM-OH)[44] in $CHCl_3$ could penetrate into the CMP cores ([PDMA-16.5k] = 0.125 equiv.) while a hydrophilic fluorophore (Alexa Fluor 647) in water could not (Figure 2h,i; Figure S43, Supporting Information). The fact that TEOA has a smaller size than PMIM-OH supports the substrate diffusion into the CMP network. To confirm that the substrate diffusion could occur within the time scale of thiol-ene coupling reaction, we compared the decays of transient absorption signals of the CMP nanoparticles ([PDMA-16.5k] = 0.125 equiv.) incubated with TEOA (0.1 M) in NMP for 1 and 24 h (Figure S44, Supporting Information). The maximum absorption signals at 600 nm and their decay kinetics were similar, regardless of the incubation time. These results indicate that the substrate diffusion into the cores was completed within 1 h. The confirmation of substrate diffusion into the CMP cores corroborates our conclusion that relative time scales of substrate diffusion and photocatalytic reactions determine the effective photocatalytic shell in the CMP nanoparticles.

One of the other possibilities to explain the size–photocatalytic reactivity relationship would be the unreacted end groups on the outer surface of CMP nanoparticles because these surface defects could be more active toward the photocatalytic reactions as suggested elsewhere.[45] However, this surface defect model predicts a linear relationship between the photocatalytic reaction rates and $6/D$, which cannot explain the reaction rates of small CMP cores (<30 nm) (Figure S45, Supporting Information). To rule out other factors, we also investigated the impacts of band structures of CMP-1-PDMAs on the photocatalytic reaction rates. The HOMO and LUMO energy levels had no correlation with the reaction rates (Figure S46, Supporting Information). Optical band gap energy showed a positive correlation with the reaction rates, but higher optical band gap energy means less light absorption by the photocatalysts in the experiments, which was not consistent with faster reaction rates (Figure S47, Supporting Information).

We also ensured that the size-dependence in the photocatalytic reactivity was not attributed to the PDMA dispersants and other impurities in the CMP-1-PDMAs. To this end, we confirmed that the PDMA dispersants were not involved in the photocatalytic reaction (Figure S48, Supporting Information) and thus, the chain lengths and the amounts of PDMA in CMP-1-PDMAs did not correlate with the CMP core size and reaction rates (Figure S49, Supporting Information). As the CMP-1-PDMAs were synthesized via palladium (Pd)-catalyzed cross-coupling reaction, residual Pd content (ppm) might correlate with the photocatalytic reactivity. As expected, we were able to detect Pd inside the CMP cores (Figures S50 and S51, Supporting Information). However, the amounts of residual Pd in all the CMP cores were ≈20 000 ppm (2 wt%) and did not show any correlation with the particle size and reaction rates (Table S17 and Figure S52, Supporting Information). This result implies that the residual Pd is not the major factor contributing to the size-dependent photocatalytic reactivity.

Lastly, smaller CMP cores may lead to larger wetted surface area, which facilitates the access of substrates to the catalytic sites and promotes the reaction kinetics.[12,46] Note that we compared wetted surface area instead of Brunauer–Emmett–Teller (BET) surface area not only because solvent-accessible surface area of CMP-1-PDMAs at room temperature is more relevant to photocatalytic performance but also because the PDMA hairs would occupy the surface of CMP-1-PDMAs in their dried state. Thus, we measured wetted surface area of CMP cores using NMR relaxometry[47,48] (Figures S53 and S54 and Tables S18 and S19, Supporting Information) and checked its impact on the reaction rates. Unexpectedly, the wetted surface area increased with the size of CMP cores (Figure S55, Supporting Information). Assuming similar microporosity in all CMP nanoparticles, we initially expected that smaller CMP cores would have larger wetted surface area because small nanoparticles have high external surface area-to-volume ratios. However, the trend implies that smaller CMP cores may not have microporosity, resulting in less wetted surface area than larger ones. This unexpected relationship between the core size and the wetted surface area indeed provided an opportunity to confirm which of core size and wetted surface area is more important factor for photocatalysis. As shown in Figure S56, Supporting Information, the wetted surface area of CMP cores was inversely correlated with the reaction rates, demonstrating that the size of CMP nanoparticles has a predominant impact on their photocatalytic reactivity. Even if we consider

© 2024 The Author(s). Advanced Materials published by Wiley-VCH GmbH

15214095, 2024, 35, Downloaded from https://onlinelibrary.wiley.com/doi/10.1002/adma.202404054 by MPI 355 Polymer Research, Wiley Online Library on [02/10/2024]. See the Terms and Conditions (https://onlinelibrary.wiley.com/terms-and-conditions) on Wiley Online Library for rules of use; OA articles are governed by the applicable Creative Commons License

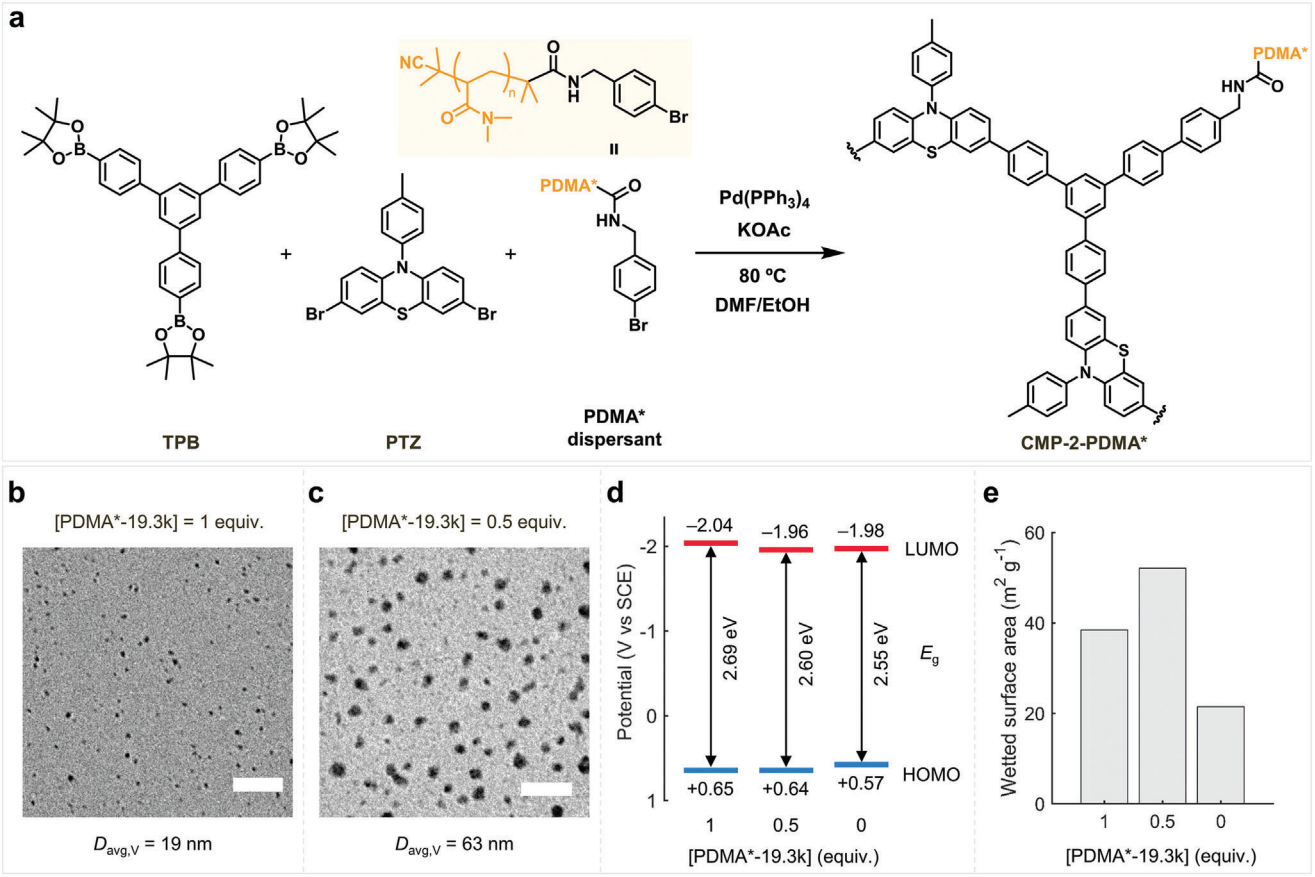

Figure 3. Size-controlled synthesis of CMP nanoparticles via Suzuki–Miyaura coupling. a) Reaction scheme for the synthesis of CMP-2-PDMA*. Different concentrations (1, 0.5, or 0 equiv.) of the PDMA* dispersant formed homogeneous mixtures with 2.5 equiv. of TPB and 3.5 equiv. of PTZ before initiating the cross-coupling reaction. KOAc: potassium acetate. See Figures S66 and S67, Supporting Information for the characterization of chemical structures of CMP-2-PDMA*s. b,c) TEM images of CMP-2-PDMA* prepared with 1 equiv. or 0.5 equiv. of PDMA*−19.3k. Scale bar: 200 nm. $D_{avg,V}$ represents the volume-weighted mean diameter. d) Band structures of CMP-2-PDMA*s. E_g is optical band gap energy. e) Wetted surface area of CMP-2-PDMA*s.

that the outer surface area of CMP cores might have been excluded in the wetted surface area measurements due to adsorbed PDMA hairs (Figure S57, Supporting Information), there was no correlation between the reaction rates and the total surface area, which was obtained by adding the wetted surface area and external surface area calculated from the core size (Figure S58, Supporting Information). After checking the aforementioned possibilities, we concluded that smaller CMP nanoparticles can provide higher photocatalytic reactivity because decreasing the particle size can reduce the dead volume of CMP nanoparticles and enable efficient use of the absorbed photons for photocatalysis.

Given that the relative time scales of substrate diffusion and photocatalytic reactions in the CMP nanoparticles determine the substrate penetration depth,[18] the size-dependent photocatalytic reactivity can be influenced by the characteristics of CMP nanoparticles and photocatalytic reactions while the general trend still holds. To demonstrate this feature, we first established dispersion polymerization conditions with Suzuki–Miyaura coupling[49] (Figures S59–S62, Supporting Information and Tables S20 and S21, Supporting Information) to synthesize different CMP nanoparticles. Notably, it was crucial to use potassium acetate as a soluble and mild base and remove the trithiocarbonate end group from the polymeric dispersant for successful Suzuki–Miyaura reactions in homogeneous conditions. With the optimized conditions, we synthesized CMP-2-PDMA*s with 1,3,5-tris(4-pinacolato-borolane-phenyl)-benzene (TPB), 3,7-dibromo-10-(*p*-tolyl)−10H-phenothiazine (PTZ), and a PDMA* dispersant (**Figure 3a**). Note that the PDMA* is the PDMA dispersant without the trithiocarbonate end group. To ensure good size control of CMP nanoparticles by changing the dispersant concentrations, we employed long chain length of PDMA* dispersant (M_n = 19.3 kg mol^{-1}) (Figures S63–S65, Supporting Information). Using this dispersant at three different concentrations (1, 0.5, and 0 equiv.), we prepared three different CMP-2-PDMA*s (Table S22, Supporting Information), which can be denoted in this paper by the concentrations (e.g., [PDMA*−19.3k] = 1 equiv.) of the dispersant used for their synthesis.

By analyzing the size and morphologies of CMP-2-PDMA*s, we verified the size-controlled synthesis of CMP nanoparticles via Suzuki–Miyaura coupling (Figure 3b,c; Figure S68, Supporting Information). The high concentration (1 equiv.) of PDMA*−19.3k produced very small nanoparticles, whose $D_{avg,V}$ was 19 nm, and lower concentration (0.5 equiv.) of PDMA*−19.3k yielded larger nanoparticles with $D_{avg,V}$ of 63 nm

© 2024 The Author(s). Advanced Materials published by Wiley-VCH GmbH

15214095, 2024, 35, Downloaded from https://onlinelibrary.wiley.com/doi/10.1002/adma.202404054 by MPI 355 Polymer Research, Wiley Online Library on [02/10/2024]. See the Terms and Conditions (https://onlinelibrary.wiley.com/terms-and-conditions) on Wiley Online Library for rules of use; OA articles are governed by the applicable Creative Commons License

(Figure S69, Supporting Information). As expected, without the dispersant, microparticles were formed (Figure S68, Supporting Information). These results clearly demonstrate that the size-controlling principle of dispersion polymerization also works for the Suzuki–Miyaura coupling reaction (Scheme 2b).

The prepared CMP-2-PDMA*s showed similar band structures (Figure 3d). The optical band gap energy (E_g) of CMP-2-PDMA*s decreased with the concentrations of the dispersant, but the values changed in the narrow range from 2.55 to 2.69 eV (Figures S70 and S71 and Table S23, Supporting Information). CV measurements revealed that the oxidation onset potential of CMP-2-PDMA*s slightly increased with the concentrations of the dispersant from +0.57 to +0.65 V vs SCE (Figure S72, Supporting Information). From the onset potential and optical band gap energy, the HOMO and LUMO energy levels of CMP-2-PDMA*s were estimated to be +0.57 to +0.65 V vs SCE and −1.96 to −2.04 V versus SCE, respectively (Tables S24 and S25, Supporting Information). These small variations in the redox potential corroborate the previous findings that the size-controlled synthesis of CMP nanoparticles did not significantly affect the electrochemical properties of the CMP cores.

Before comparing the photocatalytic reaction rates of CMP-2-PDMA*s, we also measured the weight fractions and the wetted surface area of the CMP cores. Thermogravimetric analysis revealed that lower concentrations (1, 0.5, and 0 equiv.) of the PDMA* dispersant yielded higher core weight fractions (14.1 wt%, 22.5 wt%, and 100 wt%) in CMP-2-PDMA*s (Figure S73 and Table S26, Supporting Information). The core weight fractions were used to calculate the amounts of CMP-2-PDMA*s (Table S27, Supporting Information) for preparing CMP nanoparticle dispersions, which were subject to wetted surface area measurements (Figures S74 and S75 and Table S28, Supporting Information). The wetted surface area of all CMP-2-PDMA*s were less than 60 $m^2\ g^{-1}$ and showed no correlation with the size of CMP particles (Figure 3e).

To compare the photocatalytic reactivity of CMP-2-PDMA*s, we developed photocatalytic dehalogenations of aryl halides, where a single electron transfer from the photocatalyst to an aryl halide leads to the generation of the aryl radical, which can abstract a hydrogen atom from tributylamine (TBA) to afford the product (**Figure 4a**).[50,51] This reductive dehalogenation of aryl halides is thermodynamically much more challenging than the previous thiol-ene reaction due to highly negative reduction potential of aryl halides. As a result, the dehalogenation reaction has often required photocatalysts with high reducing power such as *fac*-Ir(ppy)$_3$ (E_{ox}^* = −1.73 V vs SCE),[50,52] 10-phenylphenothiazine (E_{ox}^* = −2.1 V vs SCE),[53] and 4DP-IPN (E_{red} = −1.66 V vs SCE).[54] Considering highly negative LUMO levels (≈−2 V vs SCE), we expected that CMP-2-PDMA*s would also enable the dehalogenation of aryl halides.

Control experiments demonstrated that the transformation occurred only in the presence of both blue light and the photocatalyst, which supported the radical-based mechanism (Table S29, Supporting Information, entries 3–5). The combination of MeCN and TBA provided very good yield (81%) in the dehalogenation of iodobenzene after 24 h (entry 3 and Figure S76, Supporting Information). The same conditions achieved higher yields (88% and 97%) with more electron-deficient aryl halides, but the yields of aryl bromides decreased from 97% to 0% as the electron density in the π-system increased (Figure 4a; Figures S77–S80, Supporting Information). Interestingly, the results were consistent with the reduction potential (vs SCE) of the aryl halides: iodobenzene (−2.25 V) < 4-iodobenzonitrile (−1.80 V) < 1-bromo-2,3,5,6-tetrafluorobenzene (−1.58 V) (Figure S81, Supporting Information), indicating that the high reducing power of CMP-2-PDMA*s was vital for the one-electron reduction of the aryl halides. However, the involvement of α-aminoalkyl radicals in abstracting the halogen atom from the aryl halide[55] cannot be fully excluded, considering that the single electron transfer to iodobenzene is thermodynamically unfavorable with CMP-2-PDMA*s.

Table 1. Photocatalytic dehalogenation of iodobenzene with various photocatalysts.

Entry	Photocatalyst [0.5 mg mL^{-1}]	Reaction rates [mmol $g^{-1}\ h^{-1}$]	Yield [%]
1	CMP-2-PDMA* ([PDMA*−19.3k] = 1 equiv.)	39	81
2	Rh6G (2.1 mol%)	1	8
3	4CzIPN (1.3 mol%)	25	54
4	Biphenyl PTZ (1.7 mol%)	4	80
5	*fac*-Ir(ppy)$_3$ (1.5 mol%)	92	84

The photocatalytic reactivity of the CMP cores in CMP-2-PDMA*s was then compared by measuring the dehalogenation rates of iodobenzene after 1 h to minimize the influence of photocatalyst degradation (Figures S82 and S83, Supporting Information). The kinetic analysis showed that the photocatalytic reaction rates increased with the concentrations of the PDMA* dispersant used for the synthesis of CMP-2-PDMA*s (Figure 4b), indicating an inverse correlation between the reaction rates and the size of CMP cores (Figure 3b,c; Figure S68, Supporting Information). Particularly, the smallest CMP cores ($D_{avg,V}$ = 19 nm) achieved 2800% enhancement in the reaction rates and 500% increase in the product yields compared to the CMP microparticles ([PDMA*−19.3k] = 0 equiv.), demonstrating the potential of small CMP nanoparticles to develop energy-efficient photocatalytic transformations.

Encouraged by the dramatic impact of particle size on the photocatalytic reactivity, the smallest CMP cores were compared with other small-molecule photocatalysts in the dehalogenation reaction. Interestingly, the CMP-2-PDMA* ([PDMA*−19.3k] = 1 equiv., entry 1) achieved higher reaction rates and yields than Rh6G (entry 2) and 4CzIPN (entry 3) at the same catalyst loading (0.5 mg mL^{-1}) (**Table 1**). Although one-electron reduced Rh6G radical anion (Rh6G$^{\bullet-}$) should have sufficient reducing power (E_{ox}^* = −2.4 V vs SCE) upon blue-light excitation[56] for reducing iodobenzene, the low quantum yield for the blue-light excitation of Rh6G$^{\bullet-}$ in MeCN[57] seemed to inhibit the desired reaction. Despite its insufficient reducing power, 4CzIPN has proven its ability to catalyze dehalogenative transformations via halogen-atom transfer.[55] However, the conditions using only 1.3 mol% 4CzIPN could not compete with the smallest CMP cores. Biphenyl PTZ (entry 4), the small-molecule form of CMP-2, exhibited much slower reaction rates due to its poor solubility in MeCN. This result underscores the benefit of dispersion

© 2024 The Author(s). Advanced Materials published by Wiley-VCH GmbH

15214095, 2024, 35, Downloaded from https://onlinelibrary.wiley.com/doi/10.1002/adma.202404054 by MPI 355 Polymer Research, Wiley Online Library on [02/10/2024]. See the Terms and Conditions (https://onlinelibrary.wiley.com/terms-and-conditions) on Wiley Online Library for rules of use; OA articles are governed by the applicable Creative Commons License

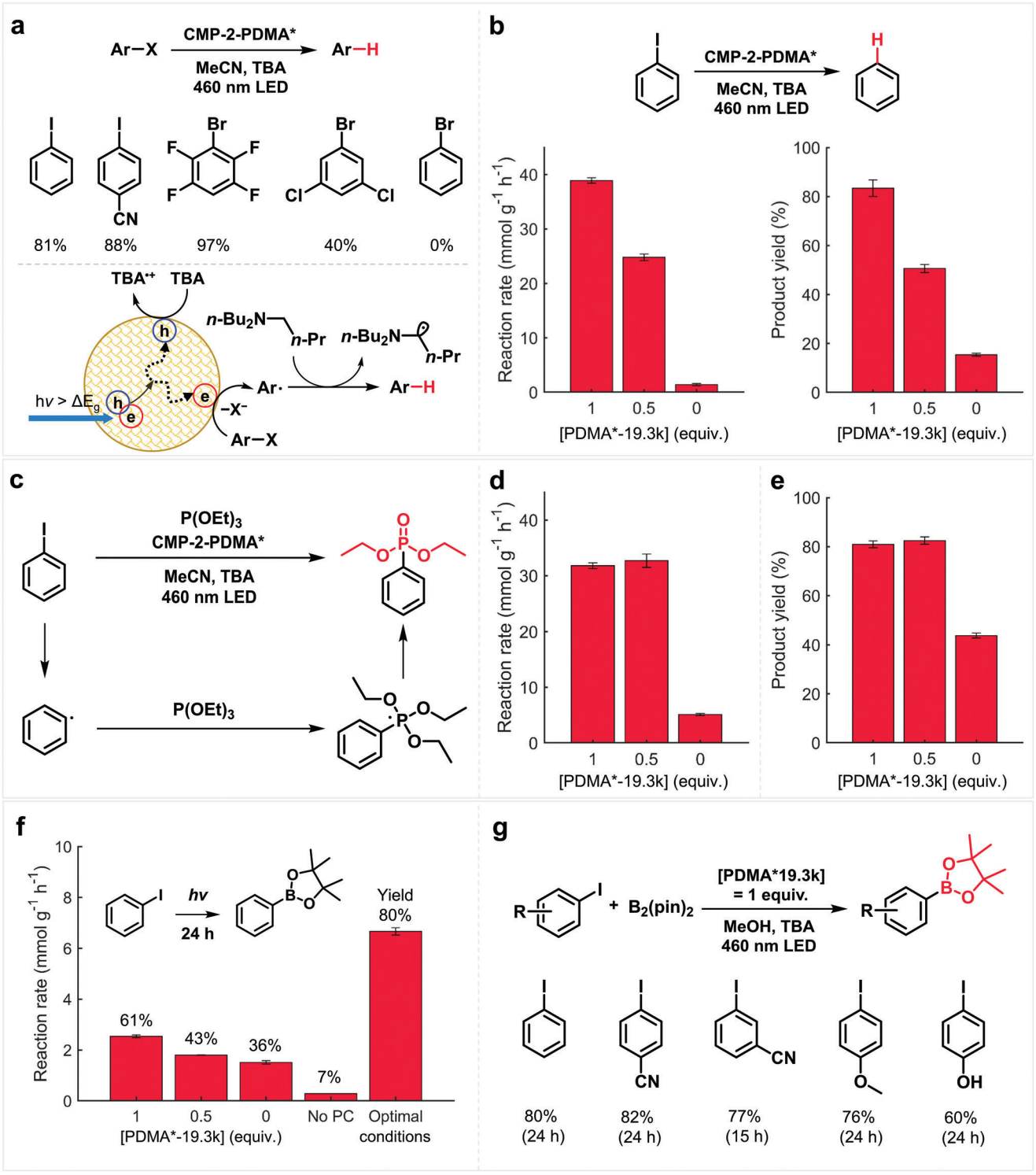

Figure 4. Photocatalytic reactivity of CMP-2-PDMA*s in photocatalytic dehalogenative transformations of aryl halides. a) Reaction scheme, substrate scope, and proposed mechanism for photocatalytic dehalogenation of aryl halides. TBA: tributylamine. b) Reaction rates per g of CMP cores (mmol g^{-1} h^{-1}) over 1 h and product yields (%) after 24 h of photocatalytic dehalogenation of iodobenzene. The error bars were obtained from three replicates. c) Reaction scheme for photocatalytic phosphonylation of iodobenzene using triethyl phosphite. d) Reaction rates per g of CMP cores (mmol g^{-1} h^{-1}) over 1 h of photocatalytic phosphonylation of iodobenzene. e) Product yields (%) after 24 h of photocatalytic phosphonylation of iodobenzene. f) Reaction rates per g of CMP cores (mmol g^{-1} h^{-1}) over 24 h and product yields of photocatalytic borylation of iodobenzene. No PC: conditions without photocatalyst. Optimal conditions: 0.1 mmol iodobenzene, 0.5 mmol TBA, 0.5 mmol $B_2(pin)_2$, and 0.5 mg CMP core of [PDMA*−19.3k] = 1 equiv. in 1 mL of MeOH. g) Reaction scheme and substrate scope for photocatalytic borylation of aryl iodides.

© 2024 The Author(s). Advanced Materials published by Wiley-VCH GmbH

15214095, 2024, 35, Downloaded from https://onlinelibrary.wiley.com/doi/10.1002/adma.202404054 by MPI 355 Polymer Research, Wiley Online Library on [02/10/2024]. See the Terms and Conditions (https://onlinelibrary.wiley.com/terms-and-conditions) on Wiley Online Library for rules of use; OA articles are governed by the applicable Creative Commons License

polymerization to synthesize well-dispersible photocatalysts with extended π-conjugation. Unfortunately, CMP-2-PDMA*s could not compete with *fac*-Ir(ppy)$_3$ (entry 5) in the dehalogenation reaction. The iridium-based polypyridyl complex achieved 92% product yield in 1 h under the same irradiation condition. This is likely because *fac*-Ir(ppy)$_3$ features high molar absorptivity, high quantum yield of long-lived triplet states, and strong reducing power (E_{ox}^{*} = −1.73 V vs SCE).[50,52] The lower photocatalytic efficiency of CMP-2-PDMA* may be attributed to poor delocalization of high energy electrons on the PTZ moiety in charge transfer states, thus decreasing the quantum yield of long-lived triplet states.[58] In this work, the *N*-aryl group of the PTZ unit was *p*-tolyl, so, replacing the electron-donating methyl (—CH_3) group with electron-withdrawing groups such as fluorine (—F) group would further stabilize the high energy electrons, increase the triplet quantum yield, and enhance the dehalogenation efficiency. In addition, constructing D–π–A structure with pyrene donor and proper π-spacer[59,60] would be a promising future direction to improve electron delocalization and charge transport across the conjugated polymer backbone for enhanced stability and photocatalytic reactivity of small CMP nanoparticles.

The reactions were conducted with 0.5 mg CMP cores or other photocatalysts, 0.05 mmol iodobenzene, and 0.25 mmol TBA in MeCN (0.05 M) under N_2 atmosphere. Blue light was irradiated using 460 nm LED at 12 mW cm^{-2}. Reaction rates were measured after 1 h of irradiation. Product yields were measured after 24 h of irradiation. For this test, 4CzIPN and 3,7-di([1,1′-biphenyl]−4-yl)−10-(*p*-tolyl)−10H-phenothiazine (biphenyl PTZ) were synthesized, as described in the Supporting Information. Rh6G and *fac*-Ir(ppy)$_3$ were obtained from commercial sources.

Given that the different sizes of CMP-2-PDMA*s have similar optical and electrochemical properties and wetted surface area (Figure 3d,e), the large enhancement in the photocatalytic reactivity with small CMP cores implies that the photocatalytic reactivity of CMP-2-PDMA*s predominantly depends on the size of CMP cores due to limited substrate accessibility to photogenerated polarons in the porous photocatalysts, as in the case of CMP-1-PDMAs. Besides, negligible effect of additional PDMA* dispersant (Figure S84, Supporting Information) and no reactivity of residual Pd (Table S30 and Figure S85, Supporting Information) in the photocatalytic dehalogenation reaction substantiate the impact of particle size on the photocatalytic reactivity of CMP-2-PDMA*s. Assuming that CMP-2-PDMA*s also have effective photocatalytic shells, we compared reaction rates of the CMP nanoparticles ([PDMA*−19.3k] = 1 equiv. and 0.5 equiv.) and estimated the shell thickness, which was 9.1 nm (Figure S86, Supporting Information). Note that almost entire parts of the smallest CMP cores ($D_{avg,V}$ = 19 nm) effectively contributed to the photocatalysis. Using the obtained shell thickness, similar calculation could be done to estimate the volume-weighted mean diameter (1.5 μm) of CMP microparticles ([PDMA*−19.3k] = 0 equiv.), which was comparable to the observed particle size (Figure S68, Supporting Information).

Next, we checked if the size-dependent photocatalytic reactivity of CMP-2-PDMA*s applies to photocatalytic phosphonylation of iodobenzene (Figure 4c). In this reaction, the aryl radical produced upon the reductive cleavage of the C—I bond is the key intermediate to react with triethyl phosphite to form C—P bonds.[61] Remarkably, the CMP nanoparticles ([PDMA*−19.3k] = 1 equiv. and 0.5 equiv.) presented almost the same reaction rates (Figure 4d) and product yields (Figure 4e) in the dehalogenative phosphonylation even though the sizes of the CMP cores were different (19 and 63 nm). In addition, the smallest CMP cores provided slightly slower phosphonylation (31.8 ± 0.5 mmol g^{-1} h^{-1}) than the hydrodehalogenation (38.9 ± 0.5 mmol g^{-1} h^{-1}), but the CMP microparticles achieved faster phosphonylation (5.1 ± 0.2 mmol g^{-1} h^{-1}) than the hydrodehalogenation (1.4 ± 0.2 mmol g^{-1} h^{-1}). By comparing the rates from the two different reactions, we speculated that the effective photocatalytic shell thickness increased due to relatively slow reaction rates in the phosphonylation and enhanced substrate diffusion in the porous photocatalysts by the addition of triethyl phosphite. Theoretically, the CMP nanoparticles with different core size (19 and 63 nm) could show similar reaction rates when the shell thickness was ≈32 nm, which allowed the whole CMP cores to be used as efficient photocatalysts under the phosphonylation conditions. Interestingly, the enhancement factor (5.1 mmol g^{-1} h^{-1}/1.4 mmol g^{-1} h^{-1} = 3.6) in the hydrodehalogenation and phosphonylation reaction rates with the CMP microparticles also agreed with the predicted value (3.4) by increasing the shell thickness from 9.1 to 32 nm in the 1.5 μm-sized CMP particles (Figure S87, Supporting Information), supporting the enhanced substrate diffusion in the porous photocatalysts with triethyl phosphite. These results corroborated the claim that the relative time scales of photocatalytic reactions and substrate diffusion in the porous photocatalysts could influence the substrate penetration depth, which accounted for the size-dependent photocatalytic reactivity of the CMP nanoparticles.

Finally, we explored photocatalytic borylation that transforms aryl iodides into aryl boronic acid pinacol esters, which are important building blocks for Suzuki–Miyaura coupling[49] and useful functional groups for drug discovery.[62] The borylation of aryl halides has been achieved via many protocols such as palladium-catalyzed cross-coupling,[63] UV-induced photochemistry,[64] and visible light photocatalysis.[65,66] Similar to the phosphonylation reaction, the photocatalytic pathways dissociate the carbon—halogen bond under mild conditions, and the resulting aryl radical reacts with bis(pinacolato)diboron ($B_2(pin)_2$) to form a C—B bond.[65,66] The fact that CMP-2-PDMA*s could generate aryl radicals from aryl iodides via the single electron transfer process provided clues about feasibility of the borylation reaction. Initial investigations started by adding 5 equiv. of $B_2(pin)_2$ to the dehalogenation condition, revealing that the smallest CMP cores ([PDMA*−19.3k] = 1 equiv.) achieved a faster reaction rate and a higher yield (61%) than larger CMP cores (Figure 4f). Without photocatalyst, the yield was only 7% after 24 h. To improve the reaction rate and yield, we tested different solvents and tertiary amines and also optimized the concentrations of reactants (Tables S31 and S32, Supporting Information). The use of MeOH as the solvent and higher concentrations of reactants (0.1 M iodobenzene, 0.5 M TBA, and 0.5 M $B_2(pin)_2$) improved the reaction rate by 260% with the same CMP cores ([PDMA*−19.3k] = 1 equiv.) and provided very good yield (80%) (Figure 4f). The optimal conditions also achieved good yields (≈80%) with electron-deficient aryl iodides bearing cyano groups and even with electron-rich aryl iodides bearing a methoxy group (Figure 4g; Figures S88–S92, Supporting Information). However,

© 2024 The Author(s). Advanced Materials published by Wiley-VCH GmbH

15214095, 2024, 35, Downloaded from https://onlinelibrary.wiley.com/doi/10.1002/adma.202404054 by MPI 355 Polymer Research, Wiley Online Library on [02/10/2024]. See the Terms and Conditions (https://onlinelibrary.wiley.com/terms-and-conditions) on Wiley Online Library for rules of use; OA articles are governed by the applicable Creative Commons License

Table 2. Photocatalytic borylation of iodobenzene with various photocatalysts.

Entry	Photocatalyst [0.5 mg mL^{-1}]	Yield$_{24\,h}$ [%]
1	CMP-2-PDMA* ([PDMA*−19.3k] = 1 equiv.)	80
2	Biphenyl PTZ (1.7 mol%)	60
3	4CzIPN (1.3 mol%)	60
4	*fac*-Ir(ppy)$_3$ (1.5 mol%)	67

the borylation of 4-iodophenol reached only 60% yield likely due to slightly more electron-donating nature of a hydroxyl group.

Remarkably, CMP-2-PDMA* ([PDMA*−19.3k] = 1 equiv.) achieved a higher yield (80%) than other photocatalysts (60–67%) in the borylation of iodobenzene at the same catalyst loading (0.5 mg mL^{-1}) (**Table 2**). Given that *fac*-Ir(ppy)$_3$ showed much better reactivity than the CMP-2-PDMA* in the dehalogenation (Table 1), we expected that *fac*-Ir(ppy)$_3$ would also provide a higher yield in the borylation reaction, but it experimentally gave a lower yield than the polymer photocatalyst. One reason for the unexpectedly low reactivity of *fac*-Ir(ppy)$_3$ is that the iridium-based photocatalyst is poorly soluble in MeOH as in the case of Biphenyl PTZ (Figure S93, Supporting Information). This result reaffirms the importance of good dispersibility of small CMP nanoparticles in developing efficient photocatalytic reactions. In addition, the dispersion polymerization protocol is compatible with a wide range of monomers and cross-coupling methods. Therefore, we anticipate that the presented synthetic strategy will enable the creation of a diverse library of highly efficient photocatalytic nanoparticles based on conjugated polymer networks.

The reactions were conducted with 0.5 mg CMP cores or other photocatalysts, 0.1 mmol iodobenzene, 0.5 mmol TBA, and 0.5 mmol $B_2(pin)_2$ in MeOH (0.1 M) under N_2 atmosphere. Blue light was irradiated using 460 nm LED at 12 mW cm^{-2}. Product yields were measured after 24 h of irradiation. Rh6G was not tested in this experiment because of its low dehalogenation yield (8%).

3. Conclusion

We have presented a dispersion polymerization strategy to synthesize well-dispersible conjugated microporous polymer (CMP) nanoparticles with controlled size. The method could control the size of CMP nanoparticles in the range from 15 to 180 nm by using different chain lengths and concentrations of polymeric dispersants while minimally affecting the photophysical and electrochemical properties of the porous photocatalysts. The photocatalytic kinetic experiments clearly demonstrated that smaller CMP nanoparticles have higher photocatalytic reactivity, even achieving more than 1000% enhancement in the photocatalytic reaction rates by decreasing the particle size. Scrutinizing the size–photocatalytic reactivity relationship, we revealed that photocatalytic reactions were limited to only the thin outer shell of CMP nanoparticles due to slow substrate diffusion and fast photocatalytic reactions in the porous photocatalysts. This finding substantiates the hypothesis that decreasing the size of CMP nanoparticles can reduce the dead volume and improve the energy-efficiency of photocatalytic reactions because absorbed photons can be used more efficiently for the reactions. Furthermore, the size-dependent photocatalytic reactivity of CMP nanoparticles highlights the importance of considering the size effect when evaluating the photocatalytic reactivity of CMPs and potentially of other porous photocatalysts. We believe that the size-controlled synthesis of CMP nanoparticles can facilitate ruling out the size effect in investigating the impact of other factors on photocatalytic reactivity.

Supporting Information

Supporting Information is available from the Wiley Online Library or from the author.

Acknowledgements

This work was supported by the Max Planck Society. The authors acknowledge the help of many scientists in the institute for obtaining TEM images (C. Sieber and K. Kirchhoff), SEM image (G. Glasser), GPC data (U. Heinz, S. Seywald, and C. Rosenauer), TGA data (P. Räder), high resolution mass spectra (S. Türk), and ICP-OES data (S. Brand), and for discussions regarding confocal imaging (X. Zhu). The authors also acknowledge the Microscopy Core Facility at the Institute of Molecular Biology (IMB Mainz) for the use of the microscopes.

Open access funding enabled and organized by Projekt DEAL.

Conflict of Interest

The authors declare no conflict of interest.

Data Availability Statement

The data that support the findings of this study are available from the corresponding author upon reasonable request.

Keywords

conjugated microporous polymer, heterogeneous photocatalyst, nanoparticles, particle size, photocatalytic reactivity, photoredox catalysis

Received: March 19, 2024
Revised: June 10, 2024
Published online: July 4, 2024

[1] J.-S. M. Lee, A. I. Cooper, *Chem. Rev.* **2020**, *120*, 2171.
[2] S. Luo, Z. Zeng, G. Zeng, Z. Liu, R. Xiao, P. Xu, H. Wang, D. Huang, Y. Liu, B. Shao, Q. Liang, D. Wang, Q. He, L. Qin, Y. Fu, *J. Mater. Chem. A* **2020**, *8*, 6434.
[3] R. Li, J. Byun, W. Huang, C. Ayed, L. Wang, K. A. I. Zhang, *ACS Catal.* **2018**, *8*, 4735.
[4] Y. Xu, S. Jin, H. Xu, A. Nagai, D. Jiang, *Chem. Soc. Rev.* **2013**, *42*, 8012.
[5] R. S. Sprick, J.-X. Jiang, B. Bonillo, S. Ren, T. Ratvijitvech, P. Guiglion, M. A. Zwijnenburg, D. J. Adams, A. I. Cooper, *J. Am. Chem. Soc.* **2015**, *137*, 3265.
[6] Y. Bai, L. Wilbraham, B. J. Slater, M. A. Zwijnenburg, R. S. Sprick, A. I. Cooper, *J. Am. Chem. Soc.* **2019**, *141*, 9063.
[7] S. Luo, Z. Zeng, G. Zeng, Z. Liu, R. Xiao, P. Xu, H. Wang, D. Huang, Y. Liu, B. Shao, Q. Liang, D. Wang, Q. He, L. Qin, Y. Fu, *J. Mater. Chem. A* **2020**, *8*, 6434.

© 2024 The Author(s). Advanced Materials published by Wiley-VCH GmbH

15214095, 2024, 35, Downloaded from https://onlinelibrary.wiley.com/doi/10.1002/adma.202404054 by MPI 355 Polymer Research, Wiley Online Library on [02/10/2024]. See the Terms and Conditions (https://onlinelibrary.wiley.com/terms-and-conditions) on Wiley Online Library for rules of use; OA articles are governed by the applicable Creative Commons License

[8] R. S. Sprick, B. Bonillo, M. Sachs, R. Clowes, J. R. Durrant, D. J. Adams, A. I. Cooper, *Chem. Commun.* **2016**, *52*, 10008.
[9] Q. Xie, Y. Yang, W. Zhang, Z. Gao, X. Li, J. Tang, C. Pan, G. Yu, *Chem. Sci.* **2021**, *12*, 5631.
[10] G. Zhang, W. Ou, J. Wang, Y. Xu, D. Xu, T. Sun, S. Xiao, M. Wang, H. Li, W. Chen, C. Su, *Appl. Catal., B* **2019**, *245*, 114.
[11] R. S. Sprick, Y. Bai, A. A. Y. Guilbert, M. Zbiri, C. M. Aitchison, L. Wilbraham, Y. Yan, D. J. Woods, M. A. Zwijnenburg, A. I. Cooper, *Chem. Mater.* **2019**, *31*, 305.
[12] E. McQueen, Y. Bai, R. S. Sprick, *Nanomaterials* **2022**, *12*, 4299.
[13] P. Zhang, Z. Weng, J. Guo, C. Wang, *Chem. Mater.* **2011**, *23*, 5243.
[14] B. C. Ma, S. Ghasimi, K. Landfester, F. Vilela, K. A. I. Zhang, *J. Mater. Chem. A* **2015**, *3*, 16064.
[15] S. Kim, K. Landfester, C. T. J. Ferguson, *ACS Nano* **2022**, *16*, 17041.
[16] P. B. Weisz, *Ind. Eng. Chem. Res.* **1995**, *34*, 2692.
[17] J. Kärger, D. M. Ruthven, D. N. Theodorou, *Diffusion in Nanoporous Materials*, Wiley-VCH, Weinheim, Germany **2012**.
[18] B. A. Johnson, A. M. Beiler, B. D. McCarthy, S. Ott, *J. Am. Chem. Soc.* **2020**, *142*, 11941.
[19] Y. Tamai, H. Ohkita, H. Benten, S. Ito, *J. Phys. Chem. Lett.* **2015**, *6*, 3417.
[20] O. V. Mikhnenko, P. W. M. Blom, T. Q. Nguyen, *Energy Environ. Sci.* **2015**, *8*, 1867.
[21] S. Kawaguchi, K. Ito, *Adv. Polym. Sci.* **2005**, *175*, 299.
[22] A. J. C. Kuehne, M. C. Gather, J. Sprakel, *Nat. Commun.* **2012**, *3*, 1088.
[23] N. Anwar, A. Rix, W. Lederle, A. J. C. Kuehne, *Chem. Commun.* **2015**, *51*, 9358.
[24] B. Haehnle, K. K. Jathavedan, P. A. Schuster, M. Karg, A. J. C. Kuehne, *Macromolecules* **2021**, *54*, 6085.
[25] K. Sonogashira, Y. Tohda, N. Hagihara, *Tetrahedron Lett.* **1975**, *50*, 4467.
[26] K. Zhang, D. Kopetzki, P. H. Seeberger, M. Antonietti, F. Vilela, *Angew. Chem., Int. Ed.* **2013**, *52*, 1432.
[27] A. B. Lowe, *Polym. Chem.* **2010**, *1*, 17.
[28] E. L. Tyson, Z. L. Niemeyer, T. P. Yoon, *J. Org. Chem.* **2014**, *79*, 1427.
[29] J. Xu, C. Boyer, *Macromolecules* **2015**, *48*, 520.
[30] S. Kaur, G. Zhao, E. Busch, T. Wang, *Org. Biomol. Chem.* **2019**, *17*, 1955.
[31] E. L. Tyson, Z. L. Niemeyer, T. P. Yoon, *J. Org. Chem.* **2014**, *79*, 1427.
[32] H. Kisch, D. Bahnemann, *J. Phys. Chem. Lett.* **2015**, *6*, 1907.
[33] M. Sachs, R. S. Sprick, D. Pearce, S. A. J. Hillman, A. Monti, A. A. Y. Guilbert, N. J. Brownbill, S. Dimitrov, X. Shi, F. Blanc, M. A. Zwijnenburg, J. Nelson, J. R. Durrant, A. I. Cooper, *Nat. Commun.* **2018**, *9*, 4968.
[34] E. Frankevich, H. Ishii, Y. Hamanaka, T. Yokoyama, A. Fuji, S. Li, K. Yoshino, A. Nakamura, K. Seki, *Phys. Rev. B: Condens. Matter Mater. Phys.* **2000**, *62*, 2505.
[35] J. Guo, H. Ohkita, H. Benten, S. Ito, *J. Am. Chem. Soc.* **2009**, *131*, 16869.
[36] M. Yan, L. J. Rothberg, F. Papadimitrakopoulos, M. E. Galvin, T. M. Miller, *Phys. Rev. Lett.* **1994**, *72*, 1104.
[37] B. Kraabel, V. I. Klimov, R. Kohlman, S. Xu, H.-L. Wang, D. W. Mcbranch, *Phys. Rev. B: Condens. Matter Mater. Phys.* **2000**, *61*, 8501.
[38] X. Zhang, K. Geng, D. Jiang, G. D. Scholes, *J. Am. Chem. Soc.* **2022**, *144*, 16423.
[39] K. Thakur, B. van der Zee, G. J. A. H. Wetzelaer, C. Ramanan, P. W. M. Blom, *Adv. Opt. Mater.* **2022**, *10*, 2101784.
[40] P. A. Lane, X. Wei, Z. V. Vardeny, *Phys. Rev. B: Condens. Matter Mater. Phys.* **1997**, *56*, 4626.
[41] H. A. Mizes, E. M. Conwell, *Phys. Rev. B: Condens. Matter Mater. Phys.* **1994**, *50*, 11243.
[42] Z. An, C. Q. Wu, X. Sun, *Phys. Rev. Lett.* **2004**, *93*, 19.
[43] J. L. Bredas, G. B. Street, *Acc. Chem. Res.* **1985**, *18*, 309.
[44] Z. H. Wu, X. Zhu, Q. Yang, Y. Zagranyarski, K. Mishra, H. Strickfaden, R. P. Wong, T. Basché, K. Koynov, M. Bonn, C. Li, X. Liu, K. Müllen, *J. Am. Chem. Soc.* **2024**, *146*, 7135.
[45] K. Schwinghammer, S. Hug, M. B. Mesch, J. Senker, B. V. Lotsch, *Energy Environ. Sci.* **2015**, *8*, 3345.
[46] X. Hai, L. Fang, M. Xiong, X. Zhou, S. Wang, H. Sun, C. Su, H. Chen, *ACS Nano* **2023**, *17*, 20570.
[47] J. J. Chen, X. Kong, K. Sumida, M. A. Manumpil, J. R. Long, J. A. Reimer, *Angew. Chem., Int. Ed.* **2013**, *52*, 12043.
[48] D. Fairhurst, T. Cosgrove, S. W. Prescott, *Magn. Reson. Chem.* **2016**, *54*, 521.
[49] N. Miyaura, A. Suzuki, *Chem. Rev.* **1995**, *95*, 2457.
[50] J. D. Nguyen, E. M. D'Amato, J. M. R. Narayanam, C. R. J. Stephenson, *Nat. Chem.* **2012**, *4*, 854.
[51] S. O. Poelma, G. L. Burnett, E. H. Discekici, K. M. Mattson, N. J. Treat, Y. Luo, Z. M. Hudson, S. L. Shankel, P. G. Clark, J. W. Kramer, C. J. Hawker, J. R. de Alaniz, *J. Org. Chem.* **2016**, *81*, 7155.
[52] N. Holmberg-Douglas, D. A. Nicewicz, *Chem. Rev.* **2022**, *122*, 1925.
[53] N. Noto, S. Saito, *ACS Catal.* **2022**, *12*, 15400.
[54] Y. Kwon, J. Lee, Y. Noh, D. Kim, Y. Lee, C. Yu, J. C. Roldao, S. Feng, J. Gierschner, R. Wannemacher, M. S. Kwon, *Nat. Commun.* **2023**, *14*, 92.
[55] T. Constantin, M. Zanini, A. Regni, N. S. Sheikh, F. Juliá, D. Leonori, *Science* **2020**, *367*, 1021.
[56] I. Ghosh, B. König, *Angew. Chem., Int. Ed.* **2016**, *55*, 7676.
[57] F. Brandl, S. Bergwinkl, C. Allacher, B. Dick, *Phys. Chem. Glasses: Eur. J. Glass Sci. Technol., Part B* **2020**, *26*, 7946.
[58] S. M. Sartor, C. H. Chrisman, R. M. Pearson, G. M. Miyake, N. H. Damrauer, *J. Phys. Chem. A* **2020**, *124*, 817.
[59] C. Shu, C. Han, X. Yang, C. Zhang, Y. Chen, S. Ren, F. Wang, F. Huang, J. X. Jiang, *Adv. Mater.* **2021**, *33*, 2008498.
[60] R. Li, X. Zhang, T. Wang, C. Li, L. Luo, C. X. Cui, W. Zhang, J. C. Wang, H. Tang, R. Zhang, C. Zhang, J. X. Jiang, *Macromolecules* **2024**, *57*, 2057.
[61] R. S. Shaikh, S. J. S. Düsel, B. König, *ACS Catal.* **2016**, *6*, 8410.
[62] H. S. Ban, H. Nakamura, *Chem. Rec.* **2015**, *15*, 616.
[63] T. Ishiyama, M. Murata, N. Miyaura, *J. Org. Chem.* **1995**, *60*, 7508.
[64] A. M. Mfuh, J. D. Doyle, B. Chhetri, H. D. Arman, O. V. Larionov, *J. Am. Chem. Soc.* **2016**, *138*, 2985.
[65] M. Jiang, H. Yang, H. Fu, *Org. Lett.* **2016**, *18*, 5248.
[66] S. Jin, H. T. Dang, G. C. Haug, R. He, V. D. Nguyen, V. T. Nguyen, H. D. Arman, K. S. Schanze, O. V. Larionov, *J. Am. Chem. Soc.* **2020**, *142*, 1603.

© 2024 The Author(s). Advanced Materials published by Wiley-VCH GmbH

15214095, 2024, 35, Downloaded from https://onlinelibrary.wiley.com/doi/10.1002/adma.202404054 by MPI 355 Polymer Research, Wiley Online Library on [02/10/2024]. See the Terms and Conditions (https://onlinelibrary.wiley.com/terms-and-conditions) on Wiley Online Library for rules of use; OA articles are governed by the applicable Creative Commons License